The Impact of Alloy Chemistry on the Formation of a Silicon-Rich Subscale on Two Classes of Ferritic Steels

Paul D. Jablonski (NETL) and John Sears (URS)

Abstract

Stainless steel type 441 (UNS S 44100) is being considered for application as a Solid Oxide Fuel Cell (SOFC) interconnect material. It had been thought that Laves phase that forms in this alloy preferentially consumes the Si present in the alloy microstructure, thereby avoiding formation of a Si-rich layer at the scale/metal interface. Recent work has shown this is not the case and a Si-rich layer does indeed form at the scale/metal interface. However, this layer is significantly different from the layer that forms in other ferritic stainless steels, for example, type 430. In this present work the Si-rich layer that forms on 441ss is examined and compared to the layer that forms on several 430-type alloys with varying low levels of Si. This research has shown that even at very low levels of Si (170 ppm), a Si-rich layer begins to form on the 430-type stainless steels. However, the morphology, particularly with respect to the thickness and continuity of the Si-rich subscale that forms in alloy 441ss, is modified in comparison to non-Laves forming ferritic stainless steels and therefore, may not be as detrimental to long term SOFC performance.

Background and Introduction

Several commercial alloys have been developed for SOFC interconnect applications. These include Crofer 22 APU (ThyssenKrupp VDM), Hitachi ZMG 232 (Hitachi Metals), and Ebrite (Allegheny Ludlum), all of which form chromium-rich oxide scales under oxidizing conditions. One disadvantage of these alloys is that they are considered "specialty" alloys, due to the addition of rare earth elements and/or extra processing steps to lower Al and Si contents. As such this increases alloy cost and they are not as readily available as other ferritic stainless steels. Additionally, it has been observed that even with special processing, these alloys often contain sufficient Si to form at least a semi-continuous Si-rich subscale [22]. Several authors [23-25] have reported that 441ss can be utilized as an interconnect with good results, even though this alloy may contain up to 1 weight percent (wt%) Si [26] and yet remain within the 441ss nominal chemistry specification. Besides the usual Cr and Mn, 441ss also contains Nb and Ti and is known to form a Fe_2Nb-based Laves phase, an intermetallic with a C14 hexagonal crystal structure [27- 28]. Previous research has shown that Si preferentially partitions to this phase over the ferritic matrix [25, 29-32]. The Laves phase has also been observed to reside on ferritic grain boundaries [25, 31-33], potentially serving as a blocking agent for grain boundary diffusion [34]. More recently, Jablonski et al. [32] showed that a Si-rich phase forms at the base of the oxide scale in alloy 441ss, disputing the effectiveness of Laves phase in either scavenging Si from the matrix or blocking diffusion. It further questions the long-term viability of 441ss in interconnect applications.

The research performed herein was intended to definitively evaluate the Si-rich subscale that forms on 441ss in comparison to that which forms on comparable stainless steels such as 430ss. Furthermore, this work intends to establish the threshold level of Si above which a layer of resistive scale is expected to form.

Summary

It is generally accepted that silica subscale formation greatly increases the ASR and reduces the performance of a SOFC, and should be avoided. Therefore, the maximum allowable Si level in ferritic stainless steel in order to avoid the formation of Si-rich subscales should be zero at or as near to zero as practical based on this present investigation. However, there are many significant differences between the Si-rich subscale that forms on the 441ss and the 430ss alloys (and perhaps other ferritic stainless steels as well). The Si-rich subscale that forms on the 441ss alloy is very irregular in thickness. This provides for low resistance pathways during SOFC operation and may help explain the low long term ASR results reported by some researchers. Additionally, the Si-rich scale was found intergranularly within the Cr_2O_3 scale both as film and islands, suggesting that the interfacial energy between this phase and the Cr_2O_3 scale is lower than the Cr_2O_3/Cr_2O_3 interfacial energy. Furthermore, the Si-rich subscale that forms on the 441ss appears to be doped with Nb, which may help to reduce the ASR of the Si-rich phase since the Nb can act as an electron donor or receptor. These unique characteristics of the Si-rich scale that forms on 441ss contribute to the low electrical resistance observed on this alloy.

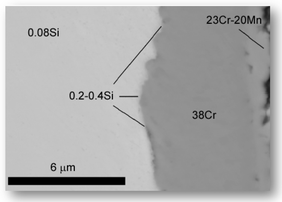

Figure 1: SEM cross section at the base metal/scale interface for alloy 430-E exposed for 2000 h at 800˚C is shown above. Note that the values are given in atomic percent and the balance is oxygen in the two outer scale layers (at right).

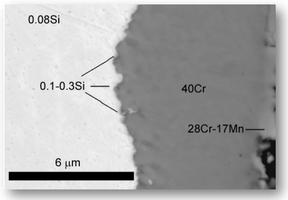

Figure 2: SEM cross section at the base metal/scale interface for alloy 430-F exposed for 2000 h at 800˚C is shown above. Note that the values are given in atomic percent and the balance is oxygen in the two outer scale layers (at right).

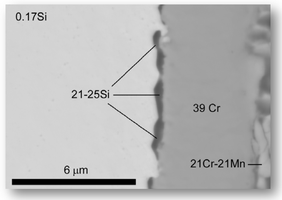

Figure 3: SEM cross section at the base metal/scale interface for alloy 430-G exposed for 2000 h at 800˚C is shown above. Note that the values are given in atomic percent and the balance is oxygen with the exception of the matrix Si level (upper left).

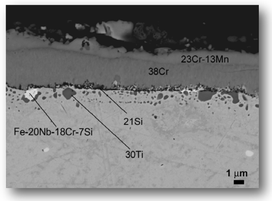

Figure 4: SEM cross section at the base metal/scale interface for alloy 441ss exposed for 2000 h at 800˚C is shown above. Note that the values are given in atomic percent and the balance is oxygen (with the exception of Laves phase which has a balance of Fe as shown).

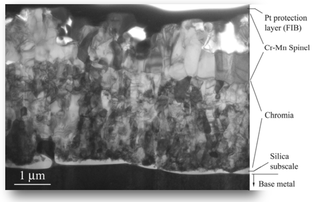

Figure 5. Low magnification TEM image of a FIB cross section taken from alloy 430-G which is representative of the FIB cross sections of each of the alloys as well as the general features of the oxide scales.

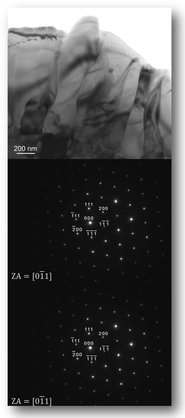

Figure 6: A TEM image of the typical outer oxide scale found on all the samples is shown above; this example is from alloy 441ss. This scale had a chemistry of 60-65 atomic percent Cr and 33-38 atomic percent Mn (metal basis) and a cubic crystal structure which identified the phase as Cr_2MnO_4 spinel. Representative diffraction patterns are also shown.

Figure 7: A TEM image of the typical inner oxide scale found on all the samples is shown above; this example is from alloy 441ss. This scale had a chemistry of essentially pure Cr (metal basis) and a triclinic crystal structure which identified the phase as Cr_2O_3. Representative diffraction patterns are also shown.

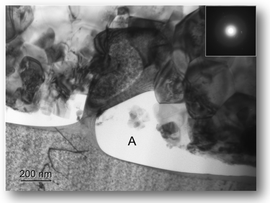

Figure 8: A TEM image of the typical oxide scale found beneath the Cr_2O_3 on the 430ss samples is shown above; this example is from alloy 430-G. This scale had a chemistry of 99 atomic percent Si (metal basis) and always exhibited a diffuse diffraction pattern indicating an amorphous structure (inset).

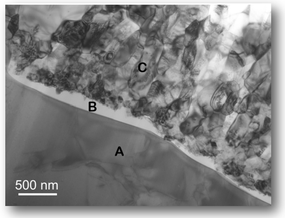

Figure 9: A TEM image of the typical oxide scale/metal region on the 430-G alloy (500 ppm Si) is shown above. Area 'A' is the matrix which had a typical alloy composition, albeit with a slight Cr depletion (Fe-16.1Cr-0.3Si-0.4Mn, weight percent). Area 'B' was Si-rich with some Cr and Fe, presumably from the surrounding regions (Si-7.6Cr-2.5Fe,atomic percent, metal basis). Area 'C' is the chromia scale (Cr-1.0Fe-2.4Mn 0.7Si, atomic percent, metal basis).

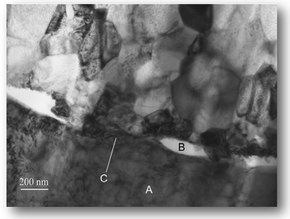

Figure 10: A TEM image of the typical oxide scale/metal region on the 430-F alloy (240ppm Si) is shown above. Area 'A' is the matrix which had a typical alloy composition, albeit with a slight Cr and Mn depletion (Fe-14.6Cr-0.1Si-0.1Mn, weight percent). Area 'B' was Si-rich with some Cr and Fe, presumably from the surrounding regions (Si-1.0Cr-1.5Fe, atomic percent, metal basis). Area 'C' is an area midway between two Si-rich areas. This area also showed a buildup of Si (Cr-8.3Fe-3.3Mn-10.2Si, atomic percent, metal basis) with the high Cr likely coming from the adjacent chromia scale.

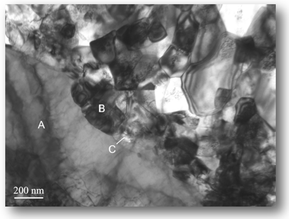

Figure 11: A TEM image of the typical oxide scale/metal region on the 430-E alloy (170ppm Si) is shown above. Area 'A' is the matrix which had a typical alloy composition, albeit with a slight Cr depletion (Fe-14.4Cr-0.2Si-0.3Mn, weight percent). Area 'B' was a chromia grain adjacent to the base alloy (Cr-1.9Fe-5.3Mn-0.8Si, atomic percent, metal basis). Area 'C' is at the chromia/alloy interface which showed a buildup of Si (Cr-2.6Fe-7.6Mn-1.8Si, atomic percent, metal basis).

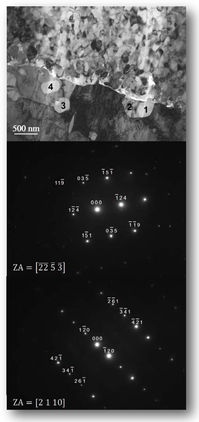

Figure 12: A TEM image of the typical oxide scale/metal region in alloy 441ss is shown above. The indicated particles were found to be Ti-rich. These particles were identified to be a Ti_4O_7 phase with a triclinic crystal structure and P-1 space group.

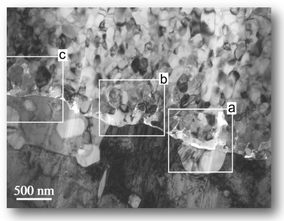

Figure 13: A TEM image of the typical oxide scale/metal region on the 441 alloy is shown above. The boxed areas are further described in subsequent figures.

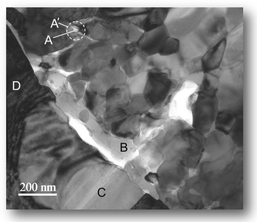

Figure 14:Figure 14: A higher magnification TEM image of boxed area 'a' from Figure 13 is shown above. A broad beam analysis of area A' gave 4.6 Si and 0.5 Nb while a narrow beam located at area A returned 12.7 Si and 1.9 Nb (atomic percent, metal basis) indicating a buildup of Si and Nb in that area.

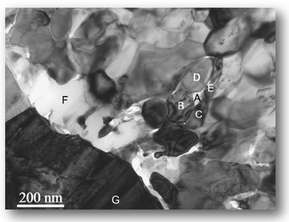

Figure 15: A higher magnification TEM image of boxed area 'b' from Figure 13 is shown above. Area F is a broad region of Si-rich sub-scale. Area G is the 441ss base metal.

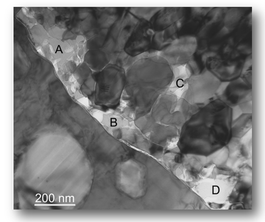

Figure 16: A higher magnification TEM image of boxed area 'c' from Figure 13 is shown above. A narrow beam analysis of the indicated areas showed that they were high in Si and Nb.

References

1 - Fuel Cell Handbook, 7th ed., EG&G Technical Services, under contract number DE-AM26-99FT40575 with US Dept of Energy, Office of Fossil Energy, National Energy Technology Laboratory, Ch 1, (2004).
2 - Mark C. Williams, Joseph P. Strakey, Wayne A. Surdoval, J of Power Sources 143 (2005) 101-196.
3 - Mark C. Williams, Joseph P. Strakey, Wayne A. Surdoval, Lane C. Wilson, Solid State Ionics, 177 (2006) 2039-2044.
4 - Mark C. Williams, Joseph P. Strakey, Wayne A. Surdoval, J of Power Sources 159 (2006) 1241-1247.
5 - S. de Souza, S.J. Visco, L.C. De Jonghe, Solid State Ionics 98 (1997) 57.
6 - H. Ishihara, H. Matsuda, Y. Takita, J. Am. Chem. Soc. 116 (1994) 3801.
7 - M. Feng, J.B. Goodenough, Eur. J. Solid State Inorg. Chem. T31 (1994) 663.
8 - P. Huang, A. Petric, J. Electrochem. Soc. 143 (5) (1996) 1644.
9 - K.Q. Huang, R. Tichy, J.B. Goodenough, J. Am. Ceram. Soc. 81 (1998) 2565.
10 - W.Z. Zhu, S.C. Deevi, Mat. Res. Bull., 38 (2003) 957-972.
11 - S.P. Simner, M.D. Anderson, G.-G. Xia, Z. Yang, L.R. Pederson, J.W. Stevenson, J. Electrochem. Soc. 152 (4) (2005) A740.
12 - M.C. Tucker, H. Kurokawa, C.P. Jacobson, L.C. De Jonghe, S.J. Visco, J. Power Sources 160 (2006) 130.
13 - M. Kumpelt, T. Kaun, T.A. Cruse, M. Hash, SECA Annual Workshop, May 11–13, 2004, available at http://www.seca.doe.gov.
14 - S.P.S. Badwal, R. Deller, K. Foger, Y. Ramprakash, J.P. Zhang, Solid State Ionics 99 (1997) 297.
15 - Y. Matsuzaki, I. Yasuda, Solid State Ionics 132 (2000) 271.
16 - S.P. Jiang, J.P. Zhand, X.G. Zheng, J. Eur. Ceram. Soc. 22 (2002) 361.
17 - Z. Yang, G. Xia, P. Singh, J.W. Stevenson, J. Power Sources 155 (2006) 246.
18 - X. Chen, P. Y. Hou, C. P. Jacobson, S. J. Visco, L. C. De Jonghe, Solid State Ionics 176 (2005) 425-433.
19 - Z. Yang, G. Xia, G. Maupin and J. Stevenson, Surface and Coatings Technology, 201(2006) 4476-4483.
20 - Z. Yang, G. Xia, X. Li and J. Stevenson, International Journal of Hydrogen Energy, 32 (2007) 3648-3654.
21 - Junwei Wu, Christopher D. Johnson, Randall S. Gemmen, and Xingbo Liu Journal of Power Sources 189 (2009) 1106.
22 - D.E. Alman, P.D. Jablonski, Int. J. Hydrogen Energy 32 (2007) 793.
23 - D. Dulieu, J. Cotton, H. Greiner, K. Honegger, A. Scholten, T. Seguelong, in: P. Stevens (Ed.), Proceedings of Third European SOFC Forum, European Solid Oxide Fuel Cell Forum, Switzerland, 1998, p. 447.
24 - S. Chandra-Ambhorn, Y. Wouters, L. Antoni, F. Toscan, A. Galerie, J. Power Sources 171 (2007) 688.
25 - Z. Yang, G. Xia, C. Wang, Z. Nie, J. Templeton, J. Stevenson, P. Singh, 183 J. Power Sources (2008) 660-667.
26 - Metals Handbook Tenth Edition, V1, Properties and Selection: Irons, Steels, and High-Performance Alloys, ASM International, Materials Park, OH, (1990) p847.
27 - in http://www.alleghenyludlum.com/ludlum/Documents/441.pdf
28 - Fe-Nb phase diagram in Binary Alloy Phase Diagrams, 2nd Ed. T.B. Massalski, editor, ASM International, Materials Park, OH, (1992) p1732.
29 - J. Froitzheim, G.H. Meier, L. Niewolak, P.J. Ennis, H. Hattendorf, L. Singheiser, W.J. Quadakkers, 178 J. Power Sources (2008) 163-173.
30 - N. Fujita, K. Ohmura, A. Yamamoto, Mat. Sci. Eng. A 359 (2003) 272-281.
31 - T. F. de Andrade, A. M. Kliauga, R. L. Plaut, A. F. Padilha, Mat. Char. 59 (2008) 503-507.
32 - P. D. Jablonski, C. J. Cowen, and J. S. Sears, J Power Sources 195 (2010) 813-820.
33 - G. M. Sim, J. C. Ahn, S. C. Hong, K. J. Lee, L. S. Lee, Mat. Sci. Eng. A 396 (2005) 159-165.
34 - T. Horita, H.Kishimoto, K. Yamaji, Y. Xiong, N. Sakai, M. E. Brito, H. Yakokawa, J. Power Sources, 176 (2008) 54-61.
35 - Jablonski and Cowen, Met Trans 40B 182 (2009).
36 - J. Rufner, P. Gannon, P. White, M. Deibert, S. Teintze, R. Smith, H. Chen, Int. J. Hyd. Eng. 33 (2008) 1392-1398.
37 - S. Geng, J. Zhu, J. Power Sources, 160 (2006) 1009-1016.
38 - S. J. Geng, J. H. Zhu, Z. G. Lu, Scripta Mat. 55 (2006) 239-242.
39 - J. Zhu, L. M. Ferdanand Diaz, G. R. Holcomb, P. D. Jablonski, C. J. Cowen, D. E. Laughlin, D. Alman, and S. Sridhar, J. Electrochem. Soc., **157** (5) B655-B664 (2010).

NATIONAL ENERGY TECHNOLOGY LABORATORY

Albany, OR • Fairbanks, AK • Morgantown, WV • Pittsburgh, PA • Sugar Land, TX